RESEARCH ARTICLE

Correspondence to:
N. Omidi,
omidi@solanasci.com

A Single Deformed Bow Shock for Titan-Saturn System

N. Omidi[1] (iD), A. H. Sulaiman[2] (iD), W. Kurth[2], H. Madanian[3] (iD), T. Cravens[3], N. Sergis[4,5] (iD), M. K. Dougherty[6], and N. J. T. Edberg[7]

[1]Solana Scientific Inc., Solana Beach, CA, USA, [2]Department of Physics and Astronomy, University of Iowa, Iowa City, IA, USA, [3]Department of Physics, University of Kansas, Lawrence, KS, USA, [4]Office for Space Research and Technology, Academy of Athens, Athens, Greece, [5]Institute for Astronomy, Astrophysics, Space Applications and Remote Sensing National Observatory of Athens, Athens, Greece, [6]Blackett Laboratory, Imperial College London, London, UK, [7]Swedish Institute of Space Physics, Uppsala, Sweden

Abstract During periods of high solar wind pressure, Saturn's bow shock is pushed inside Titan's orbit exposing the moon and its ionosphere to the solar wind. The Cassini spacecraft's T96 encounter with Titan occurred during such a period and showed evidence for shocks associated with Saturn and Titan. It also revealed the presence of two foreshocks: one prior to the closest approach (foreshock 1) and one after (foreshock 2). Using electromagnetic hybrid (kinetic ions and fluid electrons) simulations and Cassini observations, we show that the origin of foreshock 1 is tied to the formation of a single deformed bow shock for the Titan-Saturn system. We also report the observations of a structure in foreshock 1 with properties consistent with those of spontaneous hot flow anomalies formed in the simulations and previously observed at Earth, Venus, and Mars. The results of hybrid simulations also show the generation of oblique fast magnetosonic waves upstream of the outbound Titan bow shock in agreement with the observations of large-amplitude magnetosonic pulsations in foreshock 2. We also discuss the implications of a single deformed bow shock for new particle acceleration mechanisms and also Saturn's magnetopause and magnetosphere.

1. Introduction

During typical solar wind conditions, Titan's orbit falls inside Saturn's magnetosphere where it encounters the subsonic and sub-Alfvénic flow of the magnetospheric plasma (e.g., Arridge et al., 2011; Thomsen, 2013). Because of the absence of an intrinsic magnetic field at Titan, its atmosphere-ionosphere system is exposed to the surrounding plasma flow resulting in the formation of an induced magnetosphere and pickup of ionospheric ions (e.g., Coates et al., 2012; Hartle et al., 1982; Ness et al., 1982; Neubauer et al., 2006; Romanelli et al., 2014; Wei et al., 2010). During higher solar wind pressures, Saturn's magnetopause is pushed inside Titan's orbit, thereby putting Titan in the magnetosheath plasma as observed during the T32 flyby by Bertucci et al. (2008) and during T85 by Edberg et al. (2013).

It has also been thought that during sufficiently high solar wind pressures, Titan is exposed to the supersonic flow of the solar wind resulting in the formation of a bow shock for this moon separate from that of Saturn. Bertucci et al. (2015) reported Cassini's encounter with Titan (T96) during such an event and observed outbound and inbound bow shock crossings associated with Saturn (OBKBS and IBKBS, respectively), as well as those associated with Titan (OBTBS and IBTBS). These observations also show the formation of an induced magnetosphere with maximum field strengths of ~20 nT.

As noted by Bertucci et al. (2015), the encounter during T96 is suggestive of strong kinetic interactions. For example, they report the presence of large-amplitude, fast magnetosonic pulses upstream of the outbound Titan bow shock indicating a highly turbulent bow shock and foreshock during the encounter. In general, compared to 1 AU the solar wind density, magnetic field, and the Alfvén velocity are smaller at Saturn resulting in high Mach number shocks and efficient acceleration of particles to high energies (e.g., Masters et al., 2016; Sulaiman et al., 2015). The objective of this study is to further understand the kinetic processes associated with the T96 encounter and thereby obtain a more complete picture of the solar wind interaction with the Titan-Saturn system. To achieve this objective, we use a tandem of Cassini observations and electromagnetic hybrid (kinetic ions and fluid electrons) simulations of the solar wind interaction with Titan-Saturn system. In section 2, we provide an overview of the Cassini observations and the hybrid model used in the study. Section 3 reports on the origin and properties of the foreshock detected between OBKBS and IBTBS and demonstrates that its origin is tied to the formation of a single, deformed bow shock for the

Titan-Saturn system. It also reports on the presence of a structure whose properties are similar to those of spontaneous hot flow anomalies (SHFAs) observed at the Earth, Venus, and Mars suggesting the universality of collisionless shock dissipation processes (Collinson et al., 2017; Omidi, Zhang, et al., 2013; Zhang et al., 2013). Section 4 focuses on the structure of the outbound Titan bow shock and the origin of the fast magnetosonic pulses that are generated by the interaction between the solar wind and the backstreaming ions upstream of the quasi-parallel shock. We also show that the formation of a single, deformed bow shock results in new and unique particle acceleration processes that are not possible at regular bow shocks. In section 5 we provide a summary and conclusions of the study.

2. Overview of the Observations and Simulation Model

To summarize the Cassini spacecraft observations during the Titan T96 encounter, Figure 1 shows data from the magnetometer (MAG) (Dougherty et al., 2004), Magnetospheric Imaging Instrument/Charge Energy Mass Spectrometer (MIMI/CHEMS) (Krimigis et al., 2004), and Radio and Plasma Wave Science (RPWS) (Gurnett et al., 2004) instruments. Figure 1a shows the (cone) angle between the magnetic field and the solar wind flow (radial) direction with negative values corresponding to the interplanetary magnetic field (IMF) pointing sunward. Figure 1b shows the IMF clock angle that is measured with respect to the Z axis in the Kronocentric Solar Orbital (KSO) coordinate system. In this system the X axis points in the sunward direction, the Z axis points northward, and the Y axis completes a right-handed coordinate system. A clock angle of 90° corresponds to IMF pointing in the +Y direction. Although the cone and clock angles are computed for the entire encounter, we only use them when Cassini is in the solar wind. Similarly, the presence of magnetic fluctuations such as ULF waves in the foreshock result in considerable level of fluctuations in these angles making it hard to determine the instantaneous direction of the IMF. However, the overall trends in these angles are used in this study to estimate the general direction of the IMF during different periods of the T96 encounter. Figure 1c shows the magnetic field strength with the black line corresponding to linear scale and the gray line to log scale. Figure 1d shows the flux of H^+ ions measured by MIMI/CHEMS, while Figure 1e shows the electric field spectrogram from RPWS with the electron cyclotron frequency superposed as a white line.

Marked in Figure 1 are the inbound and the outbound encounters with the Kronian and Titan bow shocks, as well as the foreshocks between OBKBS and IBTBS labeled foreshock 1 and between OBTBS and IBKBS labeled foreshock 2. Foreshock 1 begins at UTC ~21:30 (red dashed line labeled foreshock 1 in Figure 1) and is associated with the onset of fluctuations and turbulence in the magnetic field, enhancement of the fluxes of energetic H^+ ions, and the presence of plasma oscillations in the electric field spectrogram. Foreshock 2 is associated with the magnetosonic pulses near the OBTBS and ULF fluctuations throughout, as well as more intense fluxes of energetic H^+ ions and plasma oscillations. This difference between the two foreshocks will be discussed in section 4.

Figure 2 shows Cassini's trajectory during the T96 encounter in the Titan-centered KSO X-Z (Figure 2a) and Y-Z (Figure 2b) planes. Also shown in Figure 2b is the direction (but not the magnitude) of the Y-Z component of the IMF every half an hour based on the clock angles shown in Figure 1. It is evident in Figure 2a that the Cassini spacecraft encountered the outbound Kronian bow shock about 20 Titan radii (R_T) upstream of Titan. Foreshock 1 was first observed (at ~21:30 UTC) about 12 R_T upstream of Titan, and the IBTBS occurs roughly at 1 R_T upstream from the moon. The OBTBS and IBKBS are observed about 2.5 and 7 R_T downstream of Titan with foreshock 2 observed between these distances. Examination of Figure 2b shows that prior to 21:30 UTC the IMF lies in a plane nearly perpendicular to Cassini's trajectory and after this time the IMF rotates into a plane more closely aligned with Cassini's trajectory. This rotation coincides well with the onset of foreshock 1 which is consistent with the notion that foreshock phenomena are primarily confined to the planes that are closely aligned with that containing the IMF and solar wind velocity. In other words, the bow shock in the planes nearly perpendicular to the IMF falls in the quasi-perpendicular regime and is not associated with a foreshock.

It is evident from Figure 2 that the retreat of Saturn's bow shock past Titan occurs during the T96 encounter. This makes it necessary to better understand how a retreating bow shock interacts with Titan in order to explain the observations. To this end, we use the results from an electromagnetic hybrid (kinetic ions and fluid electrons) simulation run using the model depicted in Figure 3a. The basics of the hybrid simulations are described in Winske and Omidi (1993, 1996). The 2.5-D (2-D in space and 3-D in currents and
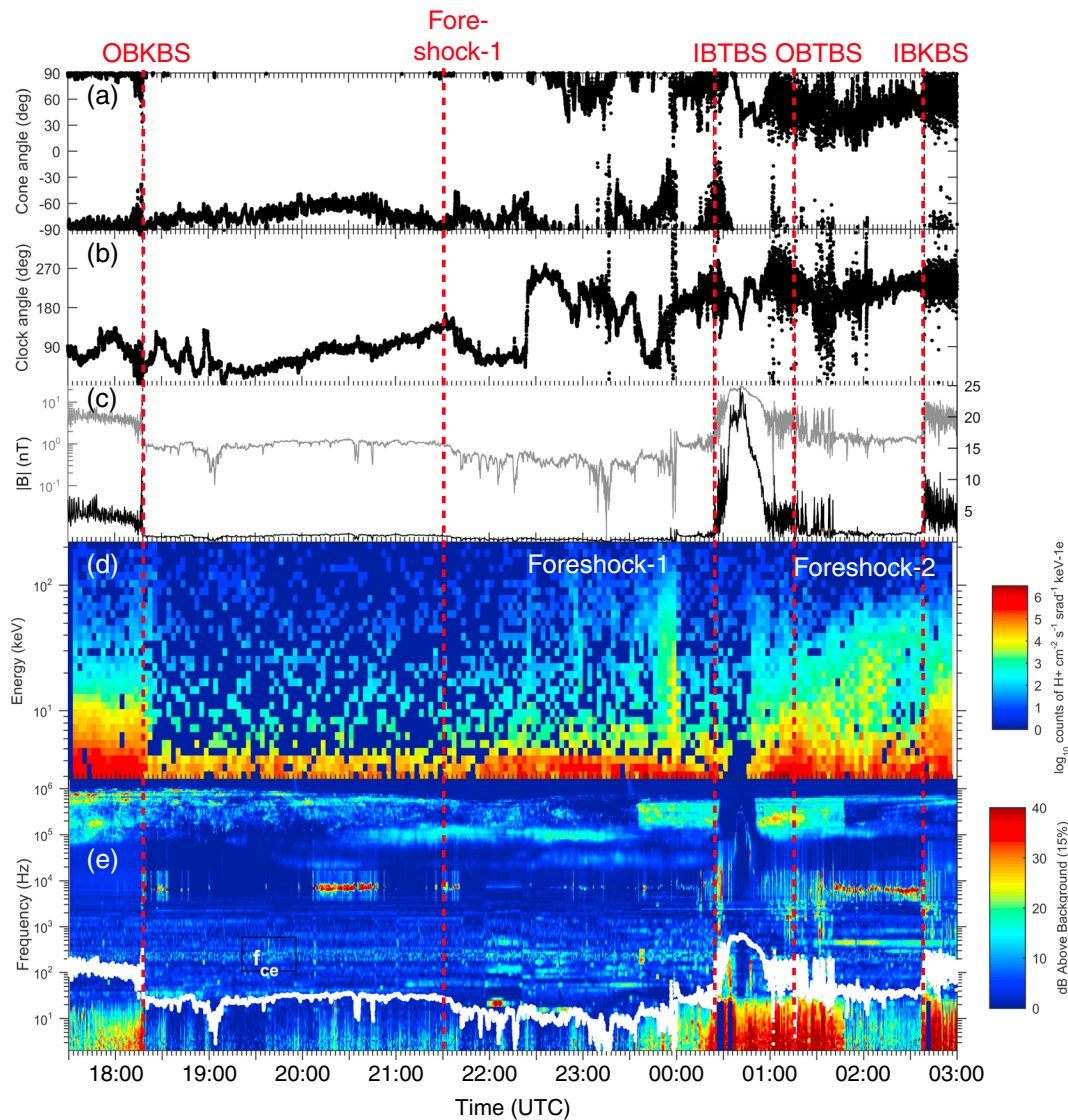
Figure 1. (a–c) The cone angle, clock angle, and total magnetic field strength, respectively, with gray line corresponding to field strength in log scale. (d) The flux of energetic H⁺ ions and (e) the electric field spectrogram with the white line indicating the electron gyrofrequency. The figure covers the entire T96 encounter.

electromagnetic fields) and 3-D versions of this model have been used in the past to study the properties of the terrestrial and Cytherean foreshocks, bow shocks, and magnetosheaths resulting in the predictions and discoveries of a number of phenomena such as foreshock cavitons (Blanco-Cano et al., 2011, 2009; Kajdič et al., 2013, 2010, 2011; Omidi, 2007), the foreshock compressional boundary (Omidi et al., 2009; Omidi, Sibeck, et al., 2013; Rojas-Castillo et al., 2013; Sibeck et al., 2008), foreshock bubbles (Omidi et al., 2010; Turner et al., 2013), spontaneous hot flow anomalies (Omidi, Zhang, et al., 2013; Zhang et al., 2013), and magnetosheath filamentary structures (Gutynska et al., 2015; Omidi, Sibeck, et al., 2014). Hybrid simulations have been utilized in the past to study solar wind interaction with Titan during the T96 encounter (Feyerabend et al., 2016). We are currently using a number of different 2.5-D and 3-D hybrid simulation models to examine the nature of the solar wind interaction with Titan and the role of the ionosphere and pickup ions on the interaction region. For the purposes of this study, the results from the model shown in Figure 3a suffice. Results from other models and their relevance to the observed locations of IBTBS and OBTBS and MIMI/CHEMS observations of pickup ions will be presented in a separate paper.

To investigate the passage of Saturn's bow shock past Titan, we use the 2.5-D hybrid simulation model shown in Figure 3a. The simulation plane X-Y contains the solar wind velocity (in the X direction) and the IMF with an
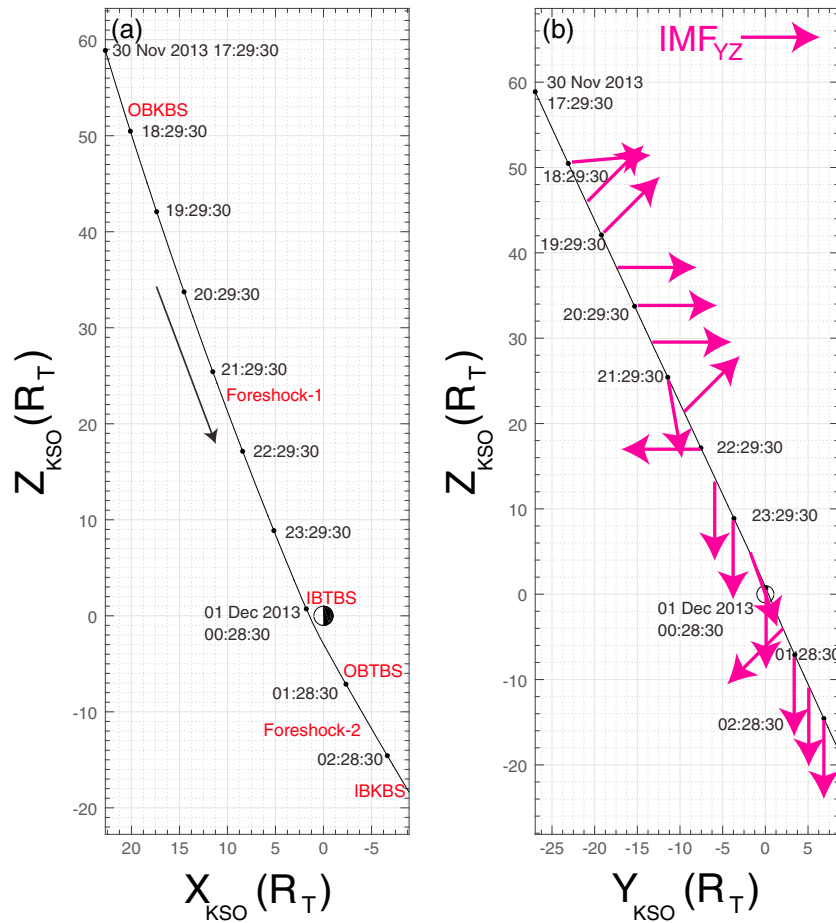
Figure 2. (a and b) The Cassini trajectory during T96 in the KSO *X-Z* and *Y-Z* planes. Figure 2a also shows the locations of shock crossings and foreshocks 1 and 2. Figure 2b also shows the direction of the *Y-Z* components of the magnetic field.

initial cone angle of −65°. We use the solar wind parameters reported by Bertucci et al. (2015), namely, number density of 0.6 cm^{-3}, velocity of 360 km/s, magnetic field strength of 0.98 nT, and ion and electron temperatures of 1 eV. This implies a proton inertial length (c/ω_p) of 290 km, where c is the speed of light and ω_p is the proton angular plasma frequency and solar wind Alfvén Mach number of 12. The simulation box extends 900 c/ω_p (100 R_T) in the X direction and 1,800 c/ω_p in the Y direction. The cell size is 1 c/ω_p in each direction with 8.1×10^7 particles in the system. The resistivity corresponds to a resistive length scale of 0.01 c/ω_p, which is much smaller than a cell size. The time step in the run is 0.00125 Ω^{-1}, where Ω is the proton angular gyrofrequency. The solar wind plasma is continuously injected from the left boundary and is allowed to leave from the remaining boundaries. Similarly, floating boundary conditions are used for the electromagnetic fields on the remaining boundaries. This implies that the electromagnetic fields on these boundaries change in time so that the excited waves and turbulence can leave the system.

Titan is centered at ($X = 400$ and $Y = 900$) and is treated as a body with a perfectly conducting ionosphere (electric field = 0), which we have found to give the same results as when an ionosphere is included in the model. This is because in both cases, ionospheric conductivity results in the pileup of IMF and the formation of a bow shock. To illustrate this point, Figures 3b and 3c show the solar wind (proton) density from two runs without and with an ionosphere model, respectively, with density normalized to its solar wind value. In these runs the simulation box is 1,000 × 1,000 proton inertial lengths. Note that in these two runs Saturn's bow shock is not included and Titan is the only obstacle to the supersonic solar wind with parameters listed above. Titan's ionospheric model is based on a simplified version of the model by Madanian et al. (2016). The model uses Cassini-Ion and Neutral Mass Spectrometer measured neutral atmosphere profiles, solar EUV irradiance fluxes, and incident magnetosheath electron fluxes to calculate electron and ion production rates. At high
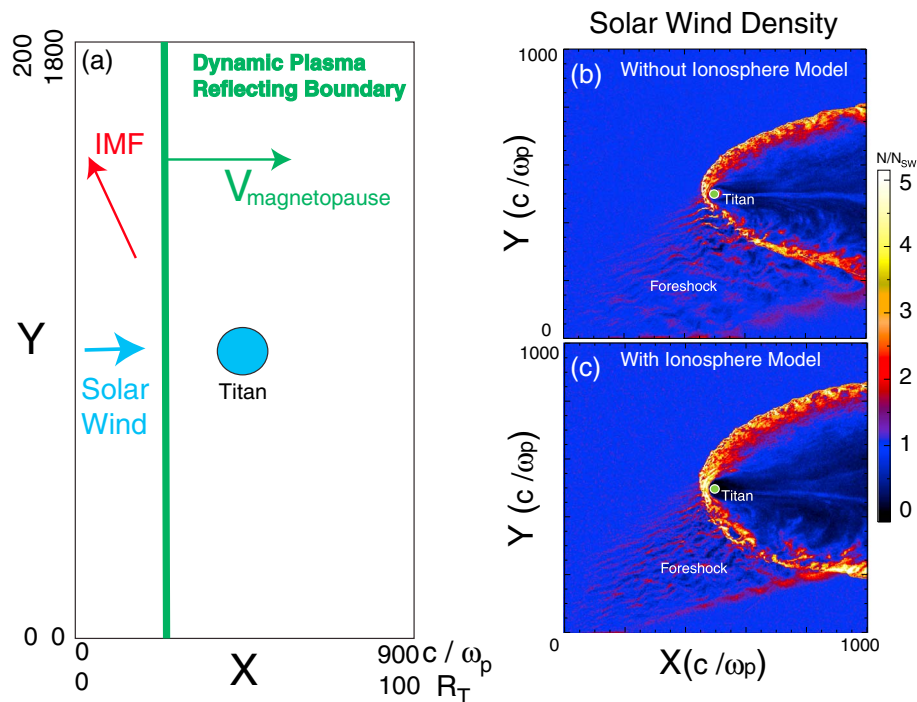
Figure 3. (a) An illustration of the hybrid simulation model used in this study. The dynamic piston is used to generate the retrieving Saturn bow shock prior to its interaction with Titan. (b) A snapshot of the density from a hybrid run without an ionosphere model and (c) the density snapshot from a run with an ionosphere model.

altitudes above 2 R_T, the hydrogen becomes the most abundant neutral species, a few times more than nitrogen. About 80% of the primary ion production comes from the photoinization, while 15–20% is produced through electron impact ionization. The total ionospheric production rate for the Hybrid model has been derived by scaling the maximum production rate near the peak of the ionosphere with respect to the relative total neutral density at higher altitude. A comparison between Figures 3b and 3c shows that the results of the runs with and without the ionosphere are very similar. Given that the extended ionosphere presents a larger obstacle than that of the body of Titan with conducting boundary conditions, the bow shock is slightly larger in Figure 3c. However, for the purposes of this study it suffices to use the model without the ionosphere. Needless to say, such a model does not address issues related to pickup of the ionospheric ions and their effects on the induced magnetosphere, which fall outside of the focus of this study. Similarly, the foreshock phenomena discussed in this paper were predicted using 2.5-D hybrid simulations and later confirmed using spacecraft observations in the Earth's foreshock. More recent 3-D hybrid simulations of the Venusian foreshock (Omidi et al., 2017) show results very similar to 2.5-D runs. As such, the use of a 2.5-D run for this study is justified given the objectives at hand. The use of a 3-D model would be required if issues related to the exact standoff position of the bow shock are under investigation.

Given the large radius of curvature (~25 Saturn radii, R_S) of Saturn's bow shock and the dimensions of the simulation box in the Y direction (~8 R_S), we can assume an initially planar shock to represent Saturn's bow shock (see, e.g., Went et al., 2011). In order to generate a retreating bow shock, we use a dynamic piston (plasma reflecting boundary) that initially falls upstream of Titan and subsequently moves in the +X direction with velocity of 3 times the Alfvén velocity (V_A). This boundary represents Saturn's magnetopause whose retreating speed is not known; however, we would expect the speeds of a few Alfvén velocities for this boundary. The results presented here and the conclusions reached in this study are not sensitive to the exact value of this speed.

3. The Origin and Properties of Foreshock 1

Our initial attempt in identifying the source of foreshock 1 met with challenges and resulted in a new model of the solar wind interaction with Titan-Saturn system that we describe in this section. Examination of the
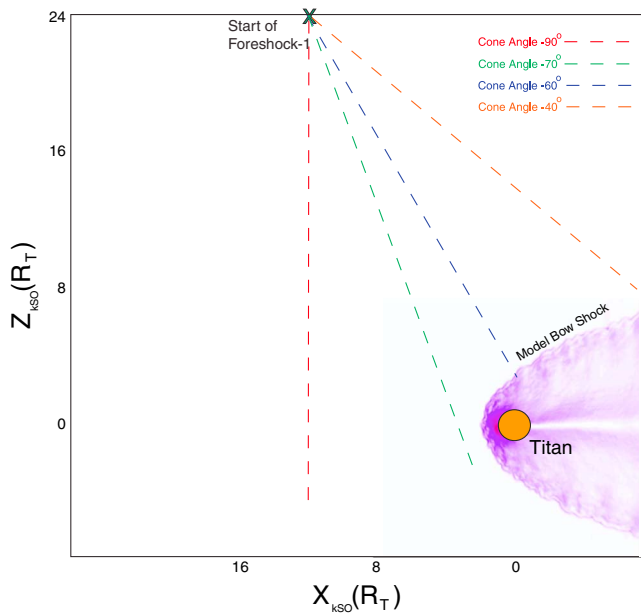
Figure 4. A model bow shock for Titan to show how IMF field lines for different cone angles passing through the point *X* intersect or do not intersect the bow shock. Point *X* corresponds to the location where foreshock 1 was first detected.

OBKBS shows that it is in the quasi-perpendicular regime with a shock normal angle of 83°, which is typical given the Parker spiral angle of the IMF (e.g., Sulaiman et al., 2016). This implies that Saturn's bow shock could not be responsible for the formation of foreshock 1 and would leave Titan as the only remaining source. However, given the direction of the IMF and the position of the IBTBS, it is not possible to account for the location and the presence of foreshock 1. To demonstrate this point, Figure 4 shows a model of the Titan bow shock in the KSO *X-Z* plane with the dayside standoff distance of the bow shock ~1 R_T upstream of the moon as indicated by the location of IBTBS. The model bow shock is generated by a hybrid simulation of the solar wind interaction with Titan (not including Saturn's bow shock) using plasma and field conditions stated in section 2. The point marked by *X* in Figure 4 indicates the location where foreshock 1 was first detected. Also shown are four interplanetary magnetic field lines that correspond to cone angles of −90°, −70°, −60°, and −40° passing through the point *X*. It is evident that for the cone angles of −90° and −70° the IMF does not connect to the bow shock and only when the cone angle is ~−60° and lower could the IMF connect to the quasi-parallel portion of Titan's bow shock. Examination of the cone angle in Figure 1 prior to and during the encounter with foreshock 1 indicates values larger than −60°, making it hard to see how Titan could account for the existence of foreshock 1.

The difficulty of explaining the origin of foreshock 1 indicates that its formation is tied to the dynamical processes associated with the retreating of Saturn's bow shock and its interaction with Titan. In order to understand the nature of this interaction better, we show results from a run using the model in Figure 3a. The four panels in Figure 5 show the plasma (proton) density normalized to solar wind value at four times during the simulation. Figure 5a shows a nearly planar shock representing the lower latitude (near the equatorial plane) portions of the Kronian bow shock with Titan and the dynamic piston located at *X* = 400 and 650, respectively. The remaining panels in Figure 5 correspond to times when the dynamic piston has moved beyond *X* = 900 and plasma is allowed to leave the system through this boundary. A basic assumption in the conceptual models of the solar wind interaction with Titan has been that the Kronian bow shock passes by Titan exposing it to the solar wind and resulting in the formation of a
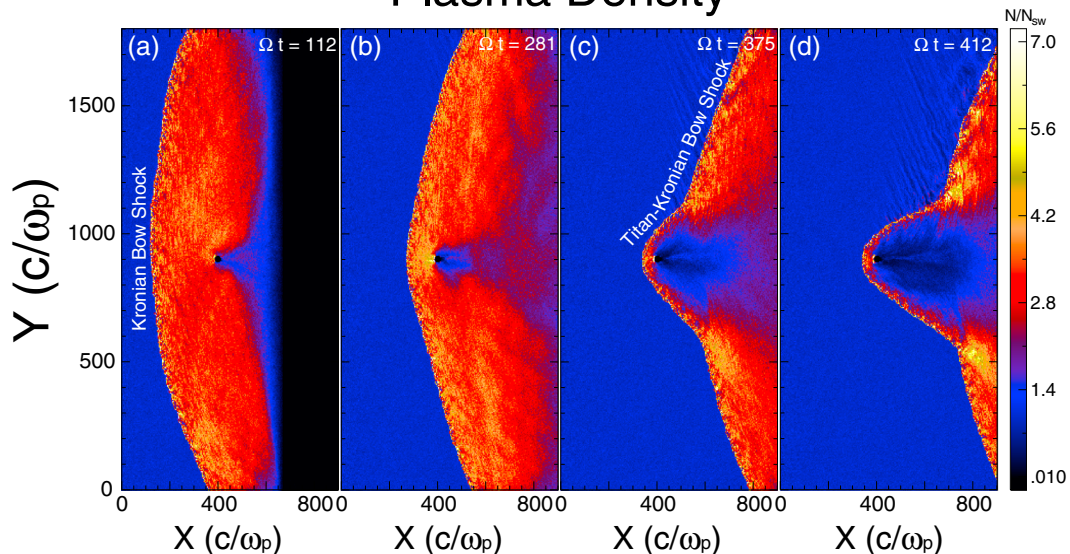
Plasma Density

Figure 5. (a–d) The number density normalized to solar wind value at four times during the simulation and demonstrate the deformation of the retrieving Kronian bow shock as it encounters Titan and transforms into a single deformed bow shock for the moon planet system.
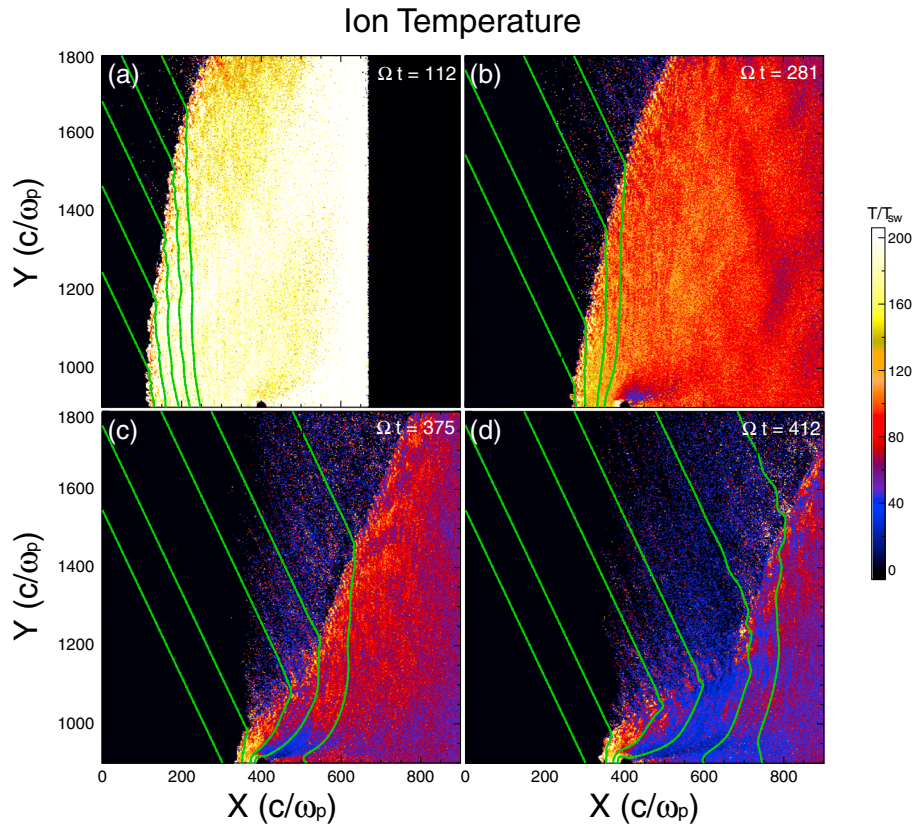
Ion Temperature

Figure 6. (a–d) The ion temperature normalized to solar wind value and IMF field lines in the upper portion of the simulation box at the same times as those in Figure 5. It is evident that the deformation of the bow shock is associated with the formation of the ion foreshock.

smaller shock for the moon. However, the results in Figure 5 indicate that, in fact, Titan adopts Saturn's bow shock as its own, resulting in the formation of a single deformed bow shock for the Titan-Saturn system. Note that the Titan portion of this deformed bow shock is similar in shape to the bow shock that would form for Titan by itself. The formation of a single deformed bow shock provides a natural explanation for the formation of foreshock 1 as described below.

Figure 6 shows the ion temperature normalized to solar wind value, as well as magnetic field lines in the upper ($Y > 900$) half of the simulation box at the same times as those in Figure 5. Ion temperature is a good way of visualizing the presence of low-density backstreaming ions in the foreshock because of their large contribution to the second moment of the velocity distribution function. Figure 6a shows the presence of a few backstreaming ions at large values of Y, where due to its curvature the shock has made a transition to quasi-parallel regime. It is evident in Figure 6 that as the bow shock becomes more deformed with time a bigger portion of it becomes quasi-parallel resulting in a bigger foreshock that extends far from Titan. As such, we attribute the origin of foreshock 1 to the ongoing deformation of the Kronian bow shock during the T96 encounter.

The formation of the foreshock in the simulation is associated with the generation and nonlinear evolution of ULF waves. In particular, according to linear theory the interaction between the backstreaming ions and the solar wind results in the generation of two classes of waves: (1) parallel propagating, circularly polarized waves with frequency below the proton cyclotron frequency and (2) oblique fast magnetosonic waves also with frequencies comparable to those of parallel propagating waves (Blanco-Cano et al., 2011). At Earth, these waves have periods of ~20–30 s and wavelengths (scale with proton skin depth) of the order of 1 R_E. Omidi (2007) used hybrid simulations to show that the coupled nonlinear evolution of these two classes of waves result in the formation of nonlinear structures called foreshock cavitons that were subsequently discovered in spacecraft data (Blanco-Cano et al., 2011, 2009; Kajdič et al., 2013, 2010, 2011). At Earth, foreshock cavitons are ~1 R_E in size, that is, comparable to the wavelength of the waves responsible for their formation. Their
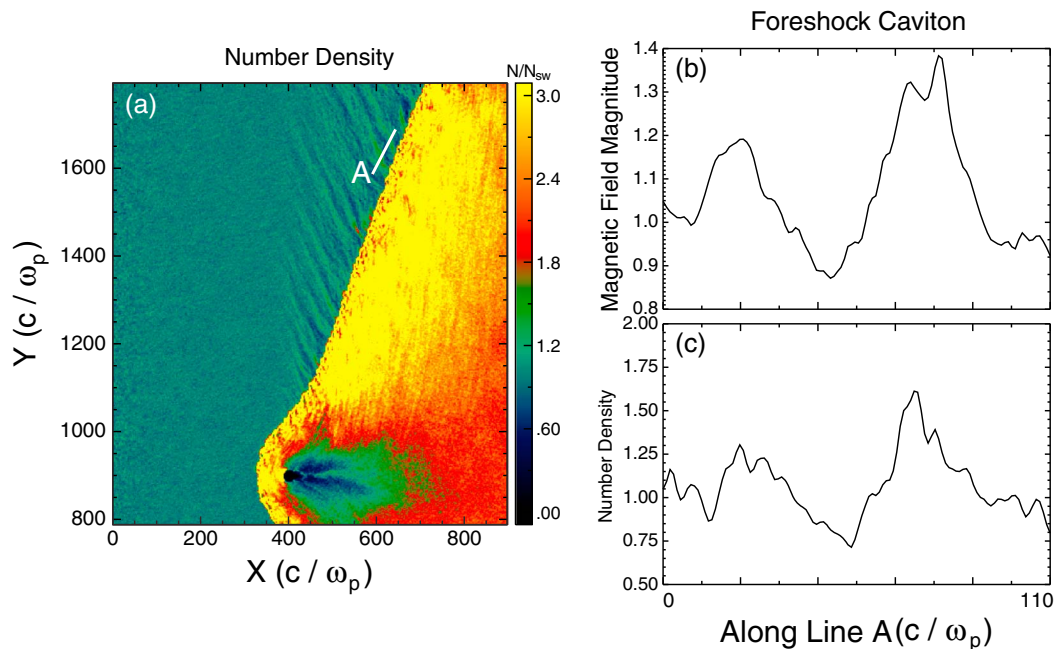
Figure 7. (a) The number density in the upper half of the simulation domain normalized to solar wind value and the color scale artificially set at 3 to make the upstream density perturbations more visible. (b and c) The variations of the total magnetic field and plasma density along the trajectory labeled "A" in Figure 7a demonstrating the formation of foreshock cavitons.

structure consists of a core of lower density and magnetic field (compared to solar wind) and rims of enhanced density and magnetic field. The velocity and temperature within the core is either slightly different from their solar wind values or basically the same.

Figure 7 shows an example of a foreshock caviton formed in the simulation during the deformation of the Kronian bow shock. Figure 7a in this figure shows the plasma density normalized to its solar wind value in the upper part of the simulation box with the scale limit artificially set at 3 to make the density fluctuations upstream of the shock more visible. Figures 7b and 7c show the variations of the total magnetic field and density (both normalized to solar wind values) along the line labeled "A" in Figure 7a. They show a structure with correlated increases (above solar wind values) in density and magnetic field at its rims and correlated decreases (below solar wind levels) in its core which match our expectations for a foreshock caviton. The size of this caviton is ~110 proton inertial lengths which correspond to ~32,000 km (~0.5 R_S), that is, considerably larger than its terrestrial counterpart due to the lower density of the solar wind at Saturn. Given the large size of Saturn's magnetosphere, the relative size of foreshock cavitons to system size is larger at Earth than Saturn.

The ULF waves responsible for the formation of foreshock cavitons are generated with their wave vector toward the Sun but are carried back by the solar wind, and as a result, foreshock cavitons are also carried toward the bow shock. Hybrid simulations and spacecraft observations at Earth's bow shock show that as foreshock cavitons approach the bow shock they further grow in amplitude and transform into structures called spontaneous hot flow anomalies (SHFAs) (Omidi, Zhang, et al., 2013; Zhang et al., 2013). This transformation is associated with larger jumps in density and magnetic field associated with the rims and a core that contains hot, decelerated and deflected solar wind plasma and energetic ions. The name spontaneous hot flow anomaly is originated from the fact that the plasma and field signatures of SHFAs in spacecraft time series data are very similar those of hot flow anomalies (HFAs) that are generated as a result of the interaction between solar wind discontinuities satisfying certain conditions and the bow shock (e.g., Burgess, 1989; Eastwood et al., 2008; Facsko et al., 2008; Jacobsen et al., 2009; Lin, 1997, 2002; Lucek et al., 2004; Masters et al., 2009; Omidi & Sibeck, 2007; Paschmann et al., 1988; Schwartz, 1995; Schwartz et al., 1988, 2000; Sibeck et al., 1999, 1998, 2000; Thomas et al., 1991; Thomsen et al., 1988, 1986, 1993; Valek et al., 2017; Zhang et al., 2010). The parametric dependencies of SHFAs have been investigated by Omidi, Zhang, et al. (2014) who showed that they form for all IMF cone angles and quasi-parallel shocks with $M_A \sim > 3$ and as such are an inherent part of the shock dissipation processes. Upon encountering the bow shock, SHFAs result in
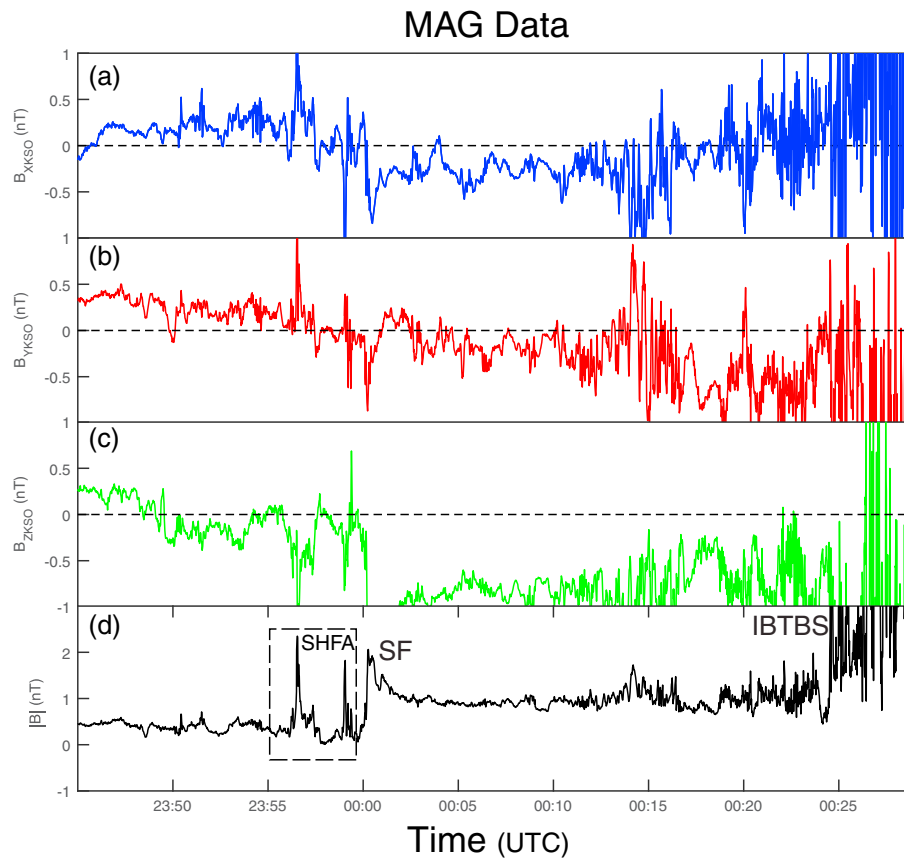
Figure 8. (a–d) The KSO *X*, *Y*, and *Z* components of magnetic field and total field strength measured by Cassini and show the presence of an SHFA in foreshock 1.

the formation of magnetosheath filamentary structures (Gutynska et al., 2015; Omidi, Sibeck, et al., 2014), magnetosheath cavities (Katriculga et al., 2009; Omidi et al., 2016), and high-speed jets in the magnetosheath (Archer et al., 2012; Hietala et al., 2009, 2012; Hietala & Plaschke, 2013; Omidi et al., 2016). In addition to the terrestrial foreshock, SHFAs have recently been observed at Venus and Mars (Collinson et al., 2017). Using 3-D hybrid simulations of the solar wind interaction with Venus, Omidi et al. (2017) show the formation of foreshock cavitons and SHFAs at Venus despite its much smaller foreshock.

The simulation results in this study indicate that SHFAs should have been formed during the T96 encounter. Figure 8 shows the magnetic field data during the time interval 23:45 to 00:30 UTC, which mostly falls in foreshock 1. Figures 8a–8c show the three components of the magnetic field in KSO coordinates, and Figure 8d shows the total field strength. The discontinuity labeled "SF" in Figure 8 was identified as an interplanetary shock by Bertucci et al. (2015), implying that it is not a part of the solar wind interaction with Titan-Saturn system. This is also consistent with the fact that foreshock 1 falls on both sides of SF. Prior to the detection of SF, Cassini encountered a structure (in the dashed box) whose magnetic signatures resemble those of HFAs and SHFAs, namely, rims associated with large enhancements of the magnetic field and a core associated with magnetic field levels below the solar wind value. To determine if this structure could be an HFA, we examine the magnetic field data for the evidence of the discontinuity needed to form the HFA. Specifically, since the observed structure is embedded or surrounded by the foreshock on both sides, we would expect to detect the responsible discontinuity within the structure (e.g., Turner et al., 2013). Examination of the magnetic field components shows no evidence for the presence of a magnetic field rotation associated with a discontinuity within the observed structure indicating that it is not an HFA. This leaves SHFA as the remaining possibility.

To provide further support for the SHFA interpretation, Figure 9 compares the observed properties of the structure with those of an SHFA generated in the hybrid run in this study. Figure 9a shows the current measured by the RPWS-LP (Langmuir) probe with changes in the current indicating variations in plasma
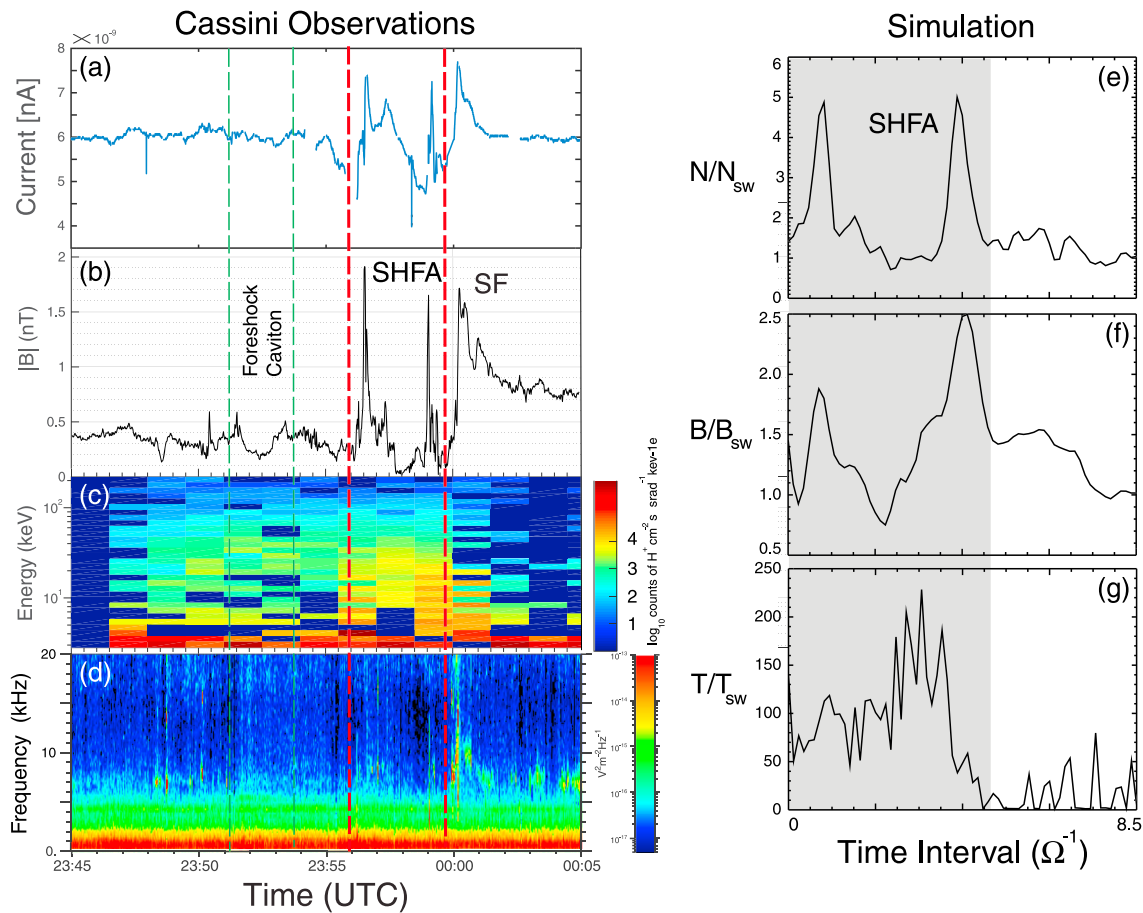
Figure 9. (a–d) LP current indicating density, magnetic field strength, flux of H$^+$ ions, and electric field spectrogram associated with the Cassini observation of an SHFA in foreshock 1. (e–g) The shaded region shows density, magnetic field strength, and ion temperature associated with a simulated SHFA. Good agreement is found between Cassini observations and hybrid simulation.

density. The LP current is collected using a fixed bias voltage on the Langmuir probe and is proportional to the electron density and also to the electron temperature (Wahlund et al., 2005). Figure 9b shows the total magnetic field strength (MAG), while Figures 9c and 9d show the fluxes of H$^+$ and electric field spectrogram from the CHEMS/MIMI and RPWS instruments respectively. The dashed red lines in the figure mark the start and end of the candidate SHFA event. The dashed green lines mark a possible foreshock caviton detected prior to the SHFA. The presence of enhanced magnetic field at the rims and reduced field in the core and the duration of the event are all consistent with a foreshock caviton interpretation. Current measurements by the LP, however, do not indicate a similar density structure, which we would expect for a foreshock caviton. Figures 9e–9g show the density, magnetic field, and ion temperature from an example SHFA upstream of the simulated Titan-Kronian bow shock. Comparing Figures 9a and 9b shows a density profile that resembles the magnetic field as expected for SHFAs and demonstrated in Figures 9e and 9f. Figure 9c shows an increase in the flux of energetic ions with energies up to 50–60 keV in the core region in agreement with our expectations for SHFAs and demonstrated in Figure 9g. Examination of the electric field spectrogram in Figure 9d shows the weak enhancement of broadband waves in the 5–10 kHz range within the candidate SHFA structure, in particular, the regions that fall within the rims. It was shown by Omidi, Zhang, et al. (2014) that regardless of solar wind velocity, the duration of SHFAs range between a few and 15 Ω^{-1}. The SHFA observed by the Cassini spacecraft lasts ~2 min that corresponds to ~6 Ω^{-1} and is consistent with the duration of the simulated SHFA in Figure 9. Given that the observed structure has properties that are consistent with those of SHFAs, we conclude that an SHFA interpretation is appropriate. Using solar wind velocity of 360 km/s, the estimated size of the observed SHFA is ~43,000 km that is about 5–6 times larger than the corresponding structures at Earth.

4. The Structure of OBTBS

Among the fascinating aspects of the T96 encounter is the observation of a series of large-amplitude, fast magnetosonic pulses upstream of the OBTBS. The presence of these pulses and ULF waves and high fluxes of energetic H^+ ions between OBTBS and IBKBS leads to its identification as a foreshock region. Examination of Figure 5 shows that for the IMF cone angle of $-65°$ the OBTBS falls in the quasi-perpendicular regime with no foreshock in the upstream region. The fact that foreshock 2 is present upstream of the OBTBS is an indication that it falls in the quasi-parallel regime and that the cone angle is no longer $-65°$. It is evident from Figure 1 that the cone angle observed during OBTBS has indeed changed from that prior to IBTBS so that it is ~35° during and after OBTBS. This change in the IMF direction needs to be accounted for in the simulation run in order to address the observations of magnetosonic pulses. To this end, we introduce a rotational discontinuity (RD) in the run that accommodates the desired change in the IMF direction resulting in the cone angle of 35°, which is comparable to the values measured by MAG. Also, given the distance of IBKBS behind Titan, we bring the dynamic piston to $X = 900$ so that Saturn's portion of the bow shock begins its sunward expansion.

Figure 10 shows the plasma density and magnetic field lines after the introduction of the RD in the run. In Figure 10a, the RD is upstream of Titan and the outbound portion of Titan's bow shock is in the quasi-perpendicular regime. Figure 10b corresponds to a time when the RD is at $X \sim 675$, and the OBTBS is in the quasi-parallel regime and a foreshock has formed as evident by the presence of large-amplitude density fluctuations upstream of the shock. In Figure 10c, Saturn's portion of the bow shock is flatter and moves sunward in quasi-parallel geometry resulting in a shock-foreshock configuration never considered in the past. In particular, north of Titan, Saturn's foreshock lies upstream of Titan's quasi-perpendicular shock while south of Titan, the foreshocks of Titan and Saturn are intermingled leading to an interesting mixture of ULF waves and energetic particles in this region.

To examine the nature of the ULF waves in the foreshock near Titan's bow shock, Figure 11a shows the density normalized to solar wind value in the lower portion of the simulation box at $t = 467 \, \Omega^{-1}$. It is evident in this panel that large-amplitude density fluctuations that connect to Titan's bow shock and extend far into the foreshock are present. They correspond to highly oblique, fast magnetosonic waves generated by the backstreaming ions in the foreshock (Blanco-Cano et al., 2011; Omidi, 2007) and are carried by the solar wind in the $+X$ direction. The point marked by "S" in Figure 11a indicates the location of a simulated spacecraft that collects plasma and field data in time. Figures 11b and 11c show the magnetic field strength and density (normalized to solar wind value) measured at point S in time and show the occurrence of correlated density and magnetic field oscillations due to the passage of the fast magnetosonic waves passed the simulated spacecraft. To compare the properties of these waves with the MAG observations of fast magnetosonic pulses upstream of the OBTBS, Figure 12 shows the three components and the total magnetic field strength from the observations and simulation. Figures 12a–12d show MAG data during 01:28–01:39 UTC and illustrate the magnetosonic pulses observed upstream of the OBTBS. A background (solar wind) magnetic field strength of 1 nT was used to convert the amplitude and durations of the simulated magnetosonic waves to those shown in Figures 12e–12h. Note the difference in the KSO and the simulation coordinate systems, in particular, in the former the X axis points sunward but in the latter it points antisunward and as a result, B_x has the opposite signs in the Cassini and simulation data. A comparison between the observations and the simulation results shows a very good agreement between the two in terms of the pulse amplitudes, durations, and the general shape of the waveforms.

As noted earlier, the deformed nature of the Titan-Saturn bow shock results in new shock-foreshock configurations that in turn lead to new particle acceleration mechanisms. Figures 13a and 13b show the density and ion temperature normalized to solar wind value and magnetic field lines at $t = 467 \, \Omega^{-1}$. From Figure 13a it is evident that at north of Titan, Saturn's foreshock falls upstream of Titan's quasi-perpendicular bow shock, which is highly unusual. The presence of turbulence associated with Saturn's foreshock upstream of the quasi-perpendicular bow shock leads to the new possibility of particle acceleration through a mix of Fermi and shock drift acceleration processes. Evidence for the presence of this new particle acceleration process is present in Figure 13b. Specifically, examination of this figure shows the presence of ions upstream of the quasi-perpendicular bow shock with energies beyond the levels seen in other parts of the foreshock. Another unique aspect of the deformed bow shock is the configuration of the quasi-parallel shocks
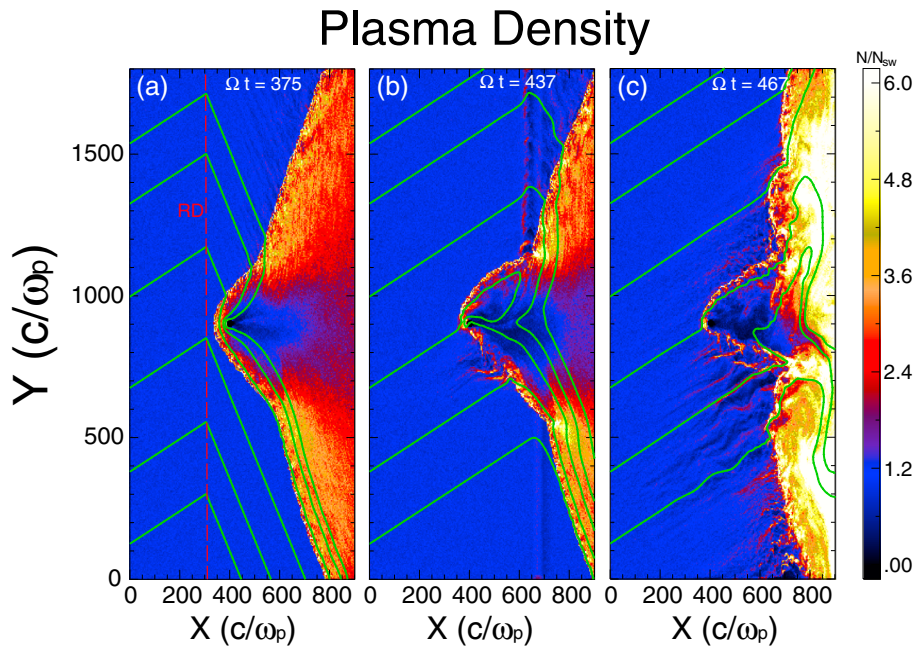
Plasma Density

Figure 10. (a–c) The plasma density and magnetic field lines at three times after the introduction of a rotational discontinuity in the simulation and demonstrates the transformation of the OBTBS from quasi-perpendicular to quasi-parallel geometries.

associated with Titan and Saturn in the southern hemisphere leading to a coupled set of foreshocks. This coupling is to some degree due to the mixing of the particles from the two foreshocks but also convection of waves and turbulence generated in Titan's foreshock into Saturn's foreshock and ultimately bow shock. Examination of foreshocks 1 and 2 in Figure 1 shows clear evidence for much stronger fluxes of energetic ions in foreshock 2. Similarly, the plasma oscillations in foreshock 2 are much stronger than those in foreshock 1. We believe that this contrast between the two foreshocks is tied to the coupled nature of foreshock 2 and the presence of energetic ions from both Titan and Saturn in this region.

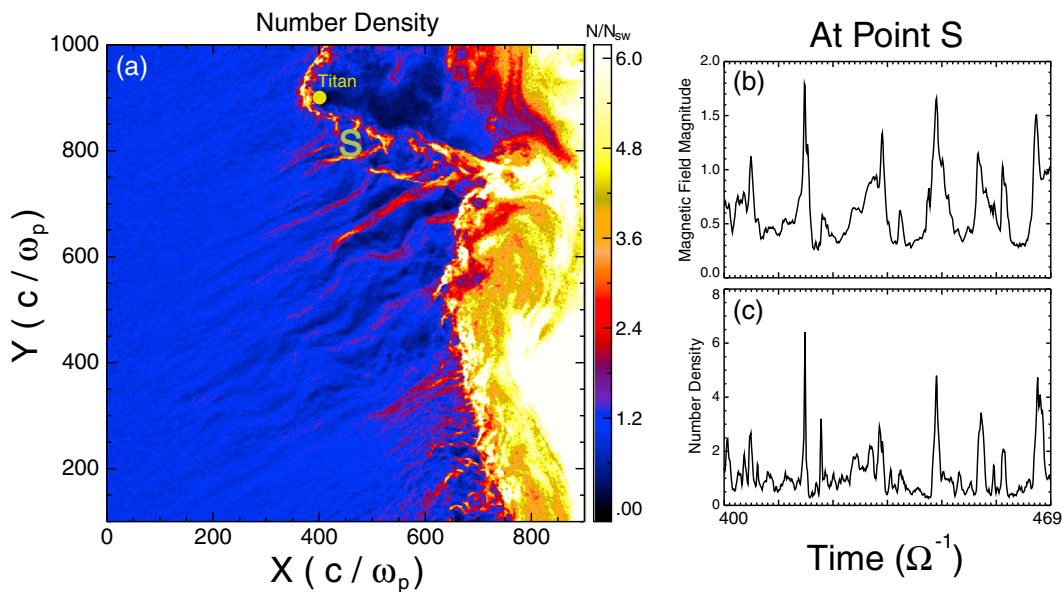**Figure 11.** (a) The number density normalized to solar wind value zoomed around the lower portion of the simulation box. (b and c) The location marked by "S" indicates the position of a simulated spacecraft measuring the magnetic field strength and density. They show correlated pulses of density and magnetic field associated with the passage of oblique fast magnetosonic waves past the simulated spacecraft.
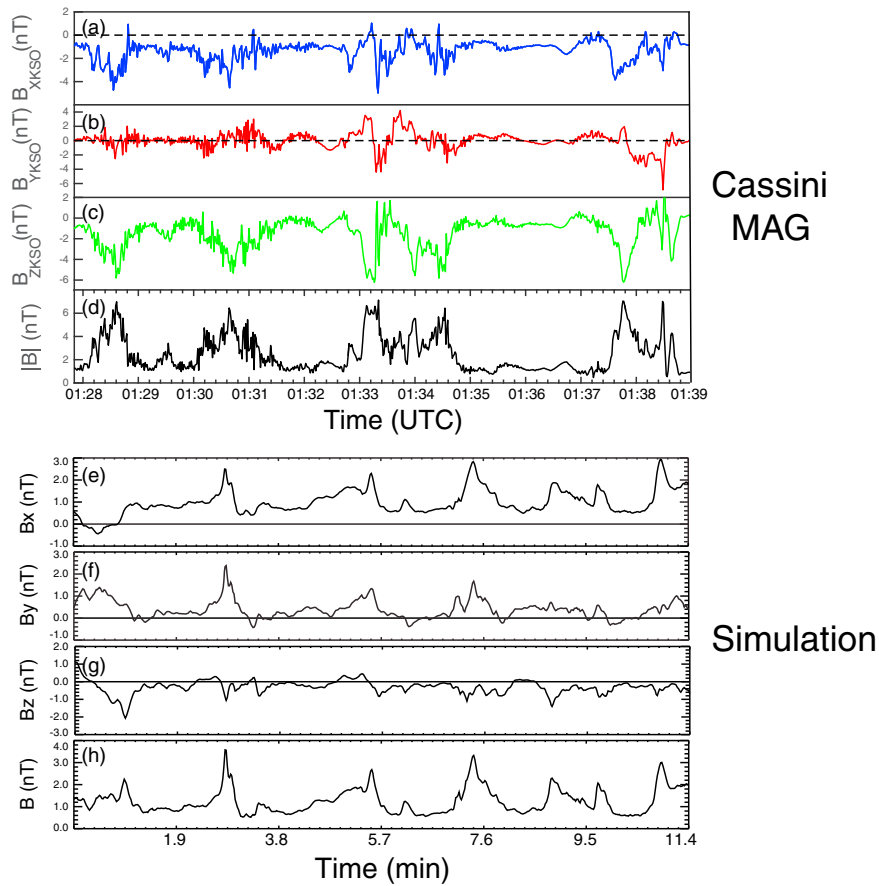
Figure 12. (a–d) MAG measurements of the KSO components of the magnetic field and field strength illustrating fast magnetosonic pulses observed upstream of the OBTBS. (e–h) The simulated magnetosonic pulses using a 1 nT background field value to convert to nanotesla. Comparing the amplitudes, durations, and the wave forms of the observed and simulated waves shows good agreement between the two.
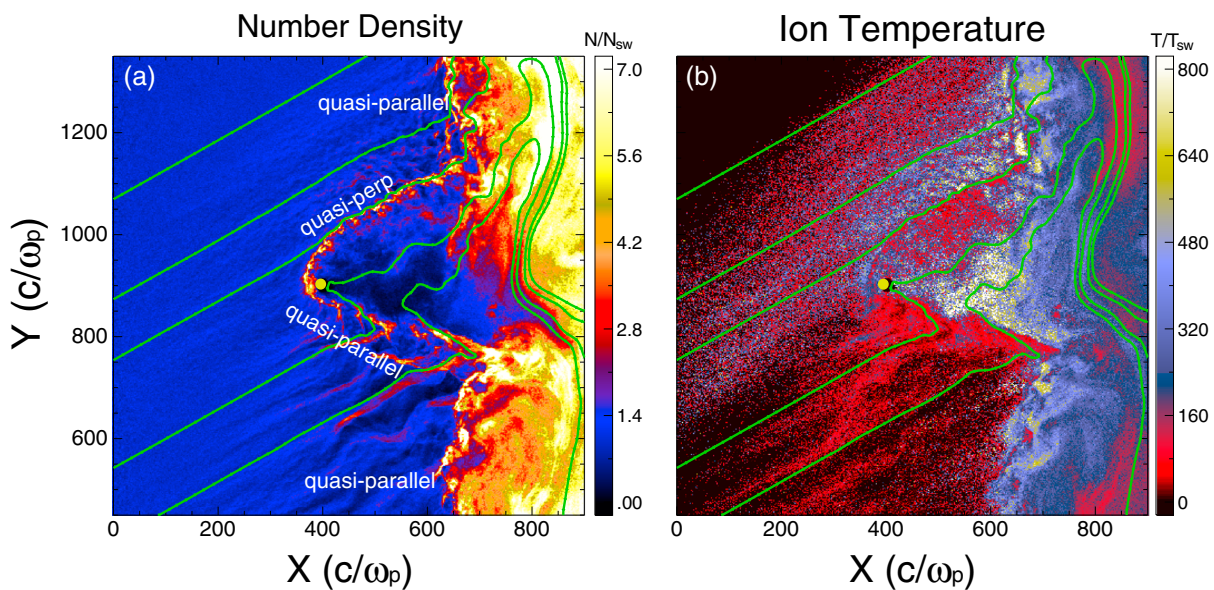

Figure 13. (a) The plasma density normalized to solar wind value illustrating the unique shock-foreshock configurations that become possible as a result of a single deformed bow shock. (b) The ion temperature normalized to solar wind value and demonstrates the presence of high-energy ions upstream of Titan's quasi-perpendicular shock.

5. Summary and Conclusions

The Cassini spacecraft observations during the T96 encounter with Titan provide us with a unique opportunity to enhance our understanding of the solar wind interaction with the Titan-Saturn system. As noted by Bertucci et al. (2015), the interaction is rich with kinetic nonlinear processes associated with ion dissipation at collisionless shocks. In this study, we have used a tandem of Cassini observations and electromagnetic hybrid simulations to better understand the nature and origin of these processes and their implications for the global picture of the solar wind interaction with Titan-Saturn system. Observations provide evidence for the existence of outbound and inbound pairs of shock crossings associated with each Titan and Saturn. This seemingly confirmed the expectation of a separate bow shock and induced magnetosphere associated with the solar wind interaction with Titan. In addition to shock crossings, Cassini also shows the presence of foreshock 1 between OBKBS and IBTBS and foreshock 2 between OBTBS and IBKBS.

Examination of the IMF cone angle and Cassini's trajectory during the T96 encounter shows that the onset of foreshock 1 coincides with the rotation of the IMF such that the plane containing the magnetic field and solar wind velocity (and therefore the foreshock) becomes more closely aligned with Cassini's trajectory. Our initial attempt to address the origin of foreshock 1 failed to establish Saturn or Titan as the source. Specifically, given the quasi-perpendicular nature of OBKBS, we can eliminate Saturn as a possibility. Using a model bow shock with nose standoff distance of 1 R_T, we examined the possibility that foreshock 1 was formed by Titan and found that for the observed cone angles of $-70°$ to $-90°$ the IMF does not intersect with Titan's bow shock. As such, it was not possible to hold Titan responsible for the formation of foreshock 1.

The difficulty in explaining the origin of foreshock 1 using static models of the bow shock and also the detection of the OBKBS upstream of Titan suggests that the formation of foreshock 1 is tied to the dynamic processes associated with the retreating of Saturn's bow shock past Titan. Using a hybrid model in which Saturn's bow shock (at low latitudes) is approximated by a planar shock formed by a retreating dynamic piston, we examined the interaction between this shock and Titan. The results show that contrary to the expectations based on the conceptual models, Saturn's bow shock does not simply retrieve past Titan leaving it exposed to the unshocked solar wind. Instead, it gets hung up on Titan, while the remainder of the bow shock continues its antisunward retreat resulting in the formation of a single deformed bow shock for the Titan-Saturn system. Examination of ion temperatures in the simulation demonstrates that the deformation of the bow shock during its retreat is associated with the transformation of the initially quasi-perpendicular shock to quasi-parallel geometry while the IMF direction remains unchanged. As such, we attribute the formation of foreshock 1 to the deformation of Saturn's bow shock as it encountered Titan.

The results of the hybrid simulation show that the interaction between the solar wind and the backstreaming ions result in the generation of parallel and oblique ULF waves with frequencies below the proton cyclotron frequency. The joint, nonlinear evolution of these waves results in the formation of foreshock cavitons, first predicted and observed in the Earth's foreshock. They consist of rims of enhanced density and magnetic fields and a core associated with lower field and plasma density. Because the size of these structures scales with the proton inertial length, foreshock cavitons are larger (~35,000 km) at Saturn where solar wind density is lower.

Foreshock cavitons are carried by the solar wind and ultimately collide with the bow shock. During this process, they grow and transform into spontaneous hot flow anomalies that consist of larger-amplitude density and magnetic field rims and cores with larger drops in density and field, containing decelerated and heated solar wind and energetic ions. A sample of the MAG data in foreshock 1 shows signatures consistent with a foreshock caviton and an SHFA although the LP measurements do not show the expected density structure for the caviton. The SHFA structure shows a density profile similar to the magnetic field and the presence of high-energy (~50 keV) H^+ ions all consistent with our expectations based on the results of hybrid simulations. Accordingly, we have concluded that an SHFA interpretation is the most likely scenario. The rim regions of this SHFA are also associated with weak enhancement of broadband 5–10 kHz waves, which diminish in the core region. Consistent with our expectations, the duration of this SHFA is ~2 min or 6 Ω^{-1}, and the size of it is ~43,000 km. The existence of SHFAs was first predicted and confirmed for the Earth's bow shock with the size of ~1 R_E and more recently at Venus and Mars with similar dimensions. Given the much lower solar wind density at Saturn, the proton inertial length is much larger resulting in

SHFAs at Saturn to be 5–6 times the size of the corresponding structures at the other three planets. Observation of SHFAs at Saturn and other planets shows the universality of ion dissipation processes at and upstream of collisionless quasi-parallel shocks.

In order to explain the Cassini observations of fast magnetosonic pulses upstream of the OBTBS, we introduced a rotational discontinuity in the hybrid model changing the IMF direction to that observed during and after the OBTBS. As expected, this changed the geometry of the OBTBS from quasi-perpendicular to quasi-parallel resulting in the formation of a foreshock with large density and magnetic field fluctuations associated with the generation of oblique fast magnetosonic waves. These waves are carried antisunward by the solar wind so that a spacecraft in this region would detect magnetosonic pulses going past the spacecraft. Comparison of the properties of the simulated and observed waves such as duration, amplitude, and general waveforms shows considerable similarity and agreement between the two.

Formation of a single deformed bow shock for the Titan-Saturn system results in shock-foreshock configurations that have not been considered in the past. This in turn leads to new particle acceleration mechanisms as demonstrated in the hybrid simulation run shown here. Specifically, during and after the OBTBS the IMF direction is such that north of Titan, its quasi-perpendicular bow shock is exposed to Saturn's foreshock that lies upstream of it. This leads to the unique possibility of accelerating particles through a combination of Fermi and shock drift acceleration processes as evident in the simulation results by the presence of high-energy ions upstream of Titan's quasi-perpendicular shock. Another unique configuration corresponds to that of foreshock 2 that falls upstream of Saturn's and Titan's quasi-parallel shocks making it a highly coupled and more intense foreshock as evident by the higher fluxes of energetic H^+ ions and more intense plasma oscillations than that of foreshock 1. Currently, the origin of these energetic ions remains unknown and future studies are needed to assess the extent to which Saturn and Titan contribute to their higher energies and fluxes. Aside from Titan, we expect other binary systems such as two planets or planet moon or other astrophysical settings to be associated with deformed bow shocks allowing for these new particle acceleration mechanisms to be operative.

Aside from foreshock processes, we expect the presence of a single deformed bow shock to have impacts on Saturn's magnetopause shape and location and the related magnetospheric consequences. In regard to the shape and location of the magnetopause, we expect the presence of a bulge on the magnetopause connected to the location of Titan's portion of the bow shock and induced magnetosphere. Based on the simulation results shown here, the size of this bulge may be 2–3 R_S given the width of Titan's portion of the bow shock. Another consequence of a single deformed bow shock is the presence of high-speed flows on the flanks of the Titan's portion of the bow shock, which encounter and penetrate the magnetosheath plasma upstream of Saturn's magnetopause. Although not shown here, examination of the flow speed in the antisunward direction from the simulation run shows the presence of supersonic flows penetrating the sheath plasma upstream of Saturn's magnetopause for 200 or more ion inertial lengths (1 R_S). The ram pressure associated with these jets can also result in local deformations of the magnetopause. Yet another impact is the presence of a complex magnetic field structure in the magnetosheath associated with Titan's induced magnetosphere and possible reconnection events at its dayside or tail. As such, we expect the formation of a single deformed bow shock to have significant impacts on Saturn's magnetopause and magnetosphere. In regard to magnetospheric impacts, the situation is somewhat similar to foreshock bubbles (Archer et al., 2015; Omidi et al., 2010; Turner et al., 2013) that also result in the outward expansion of the magnetopause and are found to significantly alter the state of the magnetosphere. In general, when Titan is on the dayside of Saturn's magnetosphere, fluctuations in the solar wind pressure may bring it into the magnetosheath (see Garnier et al., 2009), resulting in a corresponding bump on the bow shock. The size of this bump and its magnetospheric impacts increases with the elevations of the solar wind pressure and further penetration of Titan into the magnetosheath.

References

Archer, M. O., Horbury, T. S., & Eastwood, J. P. (2012). Magnetosheath pressure pulses: Generation downstream of the bow shock from solar wind discontinuities. *Journal of Geophysical Research*, 117, A05228. https://doi.org/10.1029/2011JA017468

Archer, M. O., Turner, D. L., Eastwood, J. P., Schwartz, S. J., & Horbury, T. S. (2015). Global impacts of a foreshock bubble: Magnetosheath, magnetopause and ground-based observations. *Planetary and Space Science*, 106, 56–66. https://doi.org/10.1016/j.pss.2014.11.026

Arridge, C. S., André, N., Bertucci, C. L., Garnier, P., Jackman, C. M., Németh, Z., … Crary, F. J. (2011). Upstream of Saturn and Titan. *Space Science Reviews*, *162*(1–4), 25–83. https://doi.org/10.1007/s11214-011-9849-x

Bertucci, C., Achilleos, N., Dougherty, M. K., Modolo, R., Coates, A. J., Szego, K., … Young, D. T. (2008). The magnetic memory of Titan's ionized atmosphere. *Science*, *321*(5895), 1475–1478. https://doi.org/10.1126/science.1159780

Bertucci, C., Hamilton, D. C., Kurth, W. S., Hospodarsky, G., Mitchell, D., Sergis, N., … Dougherty, M. K. (2015). Titan's interaction with the supersonic solar wind. *Geophysical Research Letters*, *42*, 193–200. https://doi.org/10.1002/2014GL062106

Blanco-Cano, X., Omidi, N., & Russell, C. T. (2009). Global hybrid simulations: Foreshock waves and cavitons under radial IMF geometry. *Journal of Geophysical Research*, *114*, A01216. https://doi.org/10.1029/2008JA013406

Blanco-Cano, X., Kajdič, P., Omidi, N., & Russell, C. T. (2011). Foreshock cavitons for different interplanetary magnetic field geometries: Simulations and observations. *Journal of Geophysical Research*, *116*, A09101. https://doi.org/10.1029/2010JA016413

Burgess, D. (1989). On the effect of a tangential discontinuity on ions specularly reflected at an oblique shock. *Journal of Geophysical Research*, *94*(A1), 472–478. https://doi.org/10.1029/JA094iA01p00472

Coates, A. J., Wellbrock, A., Lewis, G. R., Arridge, C. S., Crary, F. J., Young, D. T., … Jones, G. H. (2012). Cassini in Titan's tail: CAPS observations of plasma escape. *Journal of Geophysical Research*, *117*, A05324. https://doi.org/10.1029/2012JA017595

Collinson, G., Sibeck, D., Omidi, N., Grebowsky, J., Halekas, J., Mitchell, D., … Jakosky, B. (2017). Spontaneous hot flow anomalies at Mars and Venus. *Journal of Geophysical Research: Space Physics*, *122*, 1–14. https://doi.org/10.1002/2017JA024196

Dougherty, M., Kellock, S., Southwood, D. J., Balogh, A., Smith, E. J., Tsurutani, B. T., … Cowley, S. W. H. (2004). The Cassini magnetic field investigation. *Space Science Reviews*, *114*(1–4), 331–383. https://doi.org/10.1007/s11214-004-1432-2

Eastwood, J. P., Sibeck, D. G., Angelopoulos, V., Phan, T. D., Bale, S. D., McFadden, J. P., … Le Contel, O. (2008). THEMIS observations of a hot flow anomaly: Solar wind, magnetosheath, and ground-based measurements. *Geophysical Research Letters*, *35*, L17S03. https://doi.org/10.1029/2008GL033475

Edberg, N. J. T., Andrews, D. J., Shebanits, O., Shebanits, O., Ågren, K., Wahlund, J.-E., … Dougherty, M. K. (2013). Extreme densities in Titan's ionosphere during the T85 magnetosheath encounter. *Geophysical Research Letters*, *40*, 2879–2883. https://doi.org/10.1002/grl.50579

Facsko, G., Kecskemety, K., Erdos, G., Tatrallyay, M., Daly, P. W., & Dandouras, I. (2008). A statistical study of hot flow anomalies using Cluster data. *Advances in Space Research*, *41*(8), 1286–1291. https://doi.org/10.1016/j.asr.2008.02.005

Feyerabend, M., Simon, S., Neubauer, F. M., Motschmann, U., Bertucci, C., Edberg, N. J. T., … Kurth, W. S. (2016). Hybrid simulation of Titan's interaction with the super-sonic solar wind during Cassini's T96 flyby. *Geophysical Research Letters*, *43*, 35–42. https://doi.org/10.1002/2015GL066848

Garnier, P., Wahlund, J. E., Rosenqvist, L., Modolo, R., Ågren, K., Sergis, N., … Waite, J. H. (2009). Titan's ionosphere in the magnetosheath: Cassini RPWS results during the T32 flyby. *Annales de Geophysique*, *27*(11), 4257–4272. https://doi.org/10.5194/angeo-27-4257-2009

Gurnett, D., Kurth, W. S., Kirchner, D. L., Hospodarsky, G. B., Averkamp, T. F., Zark, P., … Pedersen, A. (2004). The Cassini radio and plasma wave investigation. *Space Science Reviews*, *114*(1–4), 395–463. https://doi.org/10.1007/s11214-004-1434-0

Gutynska, O., Sibeck, D. G., & Omidi, N. (2015). Magnetosheath plasma structures and their relation to foreshock processes. *Journal of Geophysical Research: Space Physics*, *120*, 7687–7697. https://doi.org/10.1002/2014JA020880

Hartle, R. E., Sittler, E. C. Jr., Ogilvie, K. W., Scudder, J. D., Lazarus, A. J., & Atreya, S. K. (1982). Titan's ion exosphere observed from Voyager 1. *Journal of Geophysical Research*, *87*(A3), 1383–1394. https://doi.org/10.1029/JA087iA03p01383

Hietala, H., & Plaschke, F. (2013). On the generation of magnetosheath high-speed jets by bow shock ripples. *Journal of Geophysical Research: Space Physics*, *118*, 7237–7245. https://doi.org/10.1002/2013JA019172

Hietala, H., Laitinen, T. V., Andreeova, K., Vainio, R., Vaivads, A., Palmroth, M., … Reme, H. (2009). Supermagnetosonic jets behind a collisionless quasiparallel shock. *Physical Review Letters*, *103*(24), 245,001. https://doi.org/10.1103/PhysRevLett.103.245001

Hietala, H., Partamies, N., Laitinen, T. V., Clausen, L. B. N., Facsko, G., Vaivads, A., … Lucek, E. A. (2012). Supermagnetosonic subsolar magnetosheath jets and their effects: From the solar wind to the ionospheric convection. *Annales de Geophysique*, *30*(1), 33–48. https://doi.org/10.5194/angeo-30-33-2012

Jacobsen, K. S., Phan, T. D., Eastwood, J. P., Sibeck, D. G., Moen, J. I., Angelopoulos, V., … Fornaçon, K.-H. (2009). THEMIS observations of extreme magnetopause motion caused by a hot flow anomaly. *Journal of Geophysical Research*, *114*, A10203. https://doi.org/10.1029/2008JA013873

Kajdič, P., Blanco-Cano, X., Omidi, N., & Russell, C. T. (2010). Analysis of waves surrounding the foreshock cavitons. *AIP Conference Proceedings*, *1216*, 479–482. https://doi.org/10.1063/1.3395907

Kajdič, P., Blanco-Cano, X., Omidi, N., & Russell, C. T. (2011). Multispacecraft study of foreshock cavitons. *Planetary and Space Science*, *59*(8), 705–714. https://doi.org/10.1016/j.pss.2011.%2002.005

Kajdič, P., Blanco-Cano, X., Omidi, N., Meziane, K., & Russell, C. T. (2013). Statistical study of foreshock cavitons. *Annales de Geophysique*, *31*(12), 2163–2178. https://doi.org/10.5194/angeo-31-2163-2013

Katriculga, F. T., Kaymaz, Z., Sibeck, D. G., & Dandouras, I. (2009). Magnetosheath cavities: Case studies using cluster observations. *Annales de Geophysique*, *27*, 3765–3780.

Krimigis, S., Mitchell, D. G., Hamilton, D. C., Livi, S., Dandouras, J., Jaskulek, S., … Williams, D. J. (2004). Magnetosphere Imaging Instrument (MIMI) on the Cassini mission to Saturn/Titan. *Space Science Reviews*, *114*(1–4), 233–329. https://doi.org/10.1007/s11214-004-1410-8

Lin, Y. (1997). Generation of anomalous flows near the bow shock by its interaction with interplanetary discontinuities. *Journal of Geophysical Research*, *102*(A11), 24,265–24,281. https://doi.org/10.1029/97JA01989

Lin, Y. (2002). Global hybrid simulation of hot flow anomalies near the bow shock and in the magnetosheath. *Planetary and Space Science*, *50*(5–6), 577, Symposium on Intercomparative Magetosheath Studies, Antalya, Turkey, SEP 04-08, 2000–591. https://doi.org/10.1016/S0032-0633(02)00037-5

Lucek, E. A., Horbury, T. S., & Balogh, A. (2004). Cluster observations of hot flow anomalies. *Journal of Geophysical Research*, *109*, A06207. https://doi.org/10.1029/2003JA010016

Madanian, H., Cravens, T. E., Richard, M. S., Waite, J. H. Jr., Edberg, N. J. T., Westlake, J. H., & Wahlund, J.-E. (2016). Solar cycle variations in ion composition in the dayside ionosphere of Titan. *Journal of Geophysical Research: Space Physics*, *121*, 8013–8037. https://doi.org/10.1002/2015JA022274

Masters, A., McAndrews, H. J., Steinberg, J. T., Thomsen, M. F., Arridge, C. S., Dougherty, M. K., … Coastes, A. J. (2009). Hot flow anomalies at Saturn's bow shock. *Journal of Geophysical Research*, *114*, A08217. https://doi.org/10.1029/2009JA014112

Masters, A., Sulaiman, A. H., Sergis, N., Stawarz, L., Fujimoto, M., Coates, A. J., & Dougherty, M. K. (2016). Suprathermal electrons at Saturn's bow shock. *ApJ*, *826*(1). https://doi.org/10.3847/0004-637X/826/1/48

Ness, N. F., Acuña, M. H., Behannon, K. W., & Neubauer, F. M. (1982). The induced magnetosphere of Titan. *Journal of Geophysical Research*, *87*(A3), 1369–1381. https://doi.org/10.1029/JA087iA03p01369

Neubauer, F. M., Backes, H., Dougherty, M. K., Wennmacher, A., Russell, C. T., Coates, A., … Saur, J. (2006). Titan's near magnetotail from magnetic field and electron plasma observations and modeling: Cassini flybys TA, TB, and T3. *Journal of Geophysical Research*, *111*, A10220. https://doi.org/10.1029/2006JA011676

Omidi, N. (2007). Formation of foreshock cavities. In D. Shaikh, & G. Zank (Eds.), *Turbulence and nonlinear processes in astrophysical plasmas*. *AIP Conference Proceedings* (Vol. 932, pp. 181–190). New York: American Institute of Physics Melville.

Omidi, N., & Sibeck, D. (2007). Formation of hot flow anomalies and solitary shocks. *Journal of Geophysical Research*, *112*, A01203. https://doi.org/10.1029/2006JA011663

Omidi, N., Sibeck, D., & Blanco-Cano, X. (2009). The foreshock compressional boundary. *Journal of Geophysical Research*, *114*, A08205. https://doi.org/10.1029/2008JA013950

Omidi, N., Eastwood, J. P., & Sibeck, D. G. (2010). Foreshock bubbles and their global magnetospheric impacts. *Journal of Geophysical Research*, *115*, A06204. https://doi.org/10.1029/2009JA014828

Omidi, N., Zhang, H., Sibeck, D., & Turner, D. (2013). Spontaneous hot flow anomalies at quasi-parallel shocks: 2. Hybrid simulations. *Journal of Geophysical Research: Space Physics*, *118*, 173–180. https://doi.org/10.1029/2012JA018099

Omidi, N., Sibeck, D., Blanco-Cano, X., Rojas-Castillo, D., Turner, D., Zhang, H., & Kajdič, P. (2013). Dynamics of the foreshock compressional boundary and its connection to foreshock cavities. *Journal of Geophysical Research: Space Physics*, *118*, 823–831. https://doi.org/10.1002/jgra.50146

Omidi, N., Sibeck, D., Gutynska, O., & Trattner, K. J. (2014). Magnetosheath filamentary structures formed by ion acceleration at the quasi-parallel bow shock. *Journal of Geophysical Research: Space Physics*, *119*, 2593–2604. https://doi.org/10.1002/2013JA019587

Omidi, N., Zhang, H., Chu, C., Sibeck, D., & Turner, D. (2014). Parametric dependencies of spontaneous hot flow anomalies. *Journal of Geophysical Research: Space Physics*, *119*, 9823–9833. https://doi.org/10.1002/2014JA020382

Omidi, N., Berchem, J., Sibeck, D., & Zhang, H. (2016). Impacts of spontaneous hot flow anomalies on the magnetosheath and magnetopause. *Journal of Geophysical Research: Space Physics*, *121*, 3155–3169. https://doi.org/10.1002/2015JA022170

Omidi, N., Collinson, C., & Sibeck, D. (2017). Structure and properties of the foreshock at Venus. *Journal of Geophysical Research: Space Physics*, *122*, 1–2. https://doi.org/10.1002/2017JA024180

Paschmann, G., Haerendel, G., Sckopke, N., Möbius, E., Lühr, H., & Carlson, C. W. (1988). Three-dimensional plasma structures with anomalous flow directions near the Earth's bow shock. *Journal of Geophysical Research*, *93*(A10), 11,279–11,294. https://doi.org/10.1029/JA093iA10p11279

Rojas-Castillo, D., Blanco-Cano, X., Kajdič, P., & Omidi, N. (2013). Foreshock compressional boundaries observed by Cluster. *Journal of Geophysical Research: Space Physics*, *118*, 698–715. https://doi.org/10.1029/2011JA017385

Romanelli, N., Modolo, R., Dubinin, E., Berthelier, J.-J., Bertucci, C., Wahlund, J. E., … Dougherty, M. (2014). Outflow and plasma acceleration in Titan's induced magnetotail: Evidence of magnetic tension forces. *Journal of Geophysical Research: Space Physics*, *119*, 9992–10,005. https://doi.org/10.1002/2014JA020391

Schwartz, S. J. (1995). Hot flow anomalies near the Earth's bow shock. In C. T. Russell (Ed.), *Physics of collisionless shocks* (pp. 107–116). Pergamon: Advances in Space Research.

Schwartz, S. J., Kessel, R. L., Brown, C. C., Woolliscroft, L. J. C., Dunlop, M. W., Farrugia, C. J., & Hall, D. S. (1988). An active current sheet near the Earth's bow shock. *Journal of Geophysical Research*, *93*(A10), 11,295–11,310. https://doi.org/10.1029/JA093iA10p11295

Schwartz, S. J., Paschmann, G., Sckopke, N., Bauer, T. M., Dunlop, M., Fazakerley, A. N., & Thomsen, M. F. (2000). Conditions for the formation of hot flow anomalies. *Journal of Geophysical Research*, *105*(A6), 12,639–12,650. https://doi.org/10.1029/1999JA000320

Sibeck, D., Borodkova, N., Zastenker, G., Romanov, S., & Sauvaud, J. (1998). Gross deformation of the dayside magnetopause. *Geophysical Research Letters*, *25*(4), 453–456. https://doi.org/10.1029/98GL00134

Sibeck, D. G., Borodkova, N. L., Schwartz, S. J., Owen, C. J., Kessel, R., Kokubun, S., … Zastenker, G. N. (1999). Comprehensive study of the magnetospheric response to a hot flow anomaly. *Journal of Geophysical Research*, *104*(A3), 4577–4593. https://doi.org/10.1029/1998JA900021

Sibeck, D. G., Kudela, K., Lepping, R. P., Lin, R., Nemecek, Z., Nozdrachev, M. N., … Yermolaev, Y. (2000). Magnetopause motion driven by interplanetary magnetic field variations. *Journal of Geophysical Research*, *105*(A11), 25,155–25,169. https://doi.org/10.1029/2000JA900109

Sibeck, D. G., Omidi, N., Dandouras, I., & Lucek, E. (2008). On the edge of the foreshock: Model-data comparisons. *Annales de Geophysique*, *26*(6), 1539–1544. https://doi.org/10.5194/angeo-26-1539-2008

Sulaiman, A. H., Masters, A., Dougherty, M. K., Burgess, D., Fujimoto, M., & Hospodarsky, G. B. (2015). Quasiperpendicular high Mach number shocks. *Physical Review Letters*, *115*(12), 125,001-1–125,001-5. https://doi.org/10.1103/PhysRevLett.115.125001

Sulaiman, A. H., Masters, A., & Dougherty, M. K. (2016). Characterization of Saturn's bow shock: Magnetic field observations of quasi-perpendicular shocks. *Journal of Geophysical Research: Space Physics*, *121*, 4425–4434. https://doi.org/10.1002/2016JA022449

Thomas, V., Winske, D., Thomsen, M. F., & Onsager, T. G. (1991). Hybrid simulation of the formation of a hot flow anomaly. *Journal of Geophysical Research*, *96*(A7), 11,625–11,632. https://doi.org/10.1029/91JA01092

Thomsen, M. F. (2013). Saturn's magnetospheric dynamics. *Geophysical Research Letters*, *40*, 5337–5344. https://doi.org/10.1002/2013GL057967

Thomsen, M. F., Gosling, J. T., Fuselier, S. A., Bame, S. J., & Russell, C. T. (1986). Hot diamagnetic cavities upstream of the Earth's bow shock. *Journal of Geophysical Research*, *91*(A3), 2961–2973. https://doi.org/10.1029/JA091iA03p02961

Thomsen, M. F., Gosling, J. T., Bame, S. J., Quest, K. B., Russell, C. T., & Fuselier, S. A. (1988). On the origin of hot diamagnetic cavities near the Earth's bow shock. *Journal of Geophysical Research*, *93*(A10), 11,311–11,325. https://doi.org/10.1029/JA093iA10p11311

Thomsen, M. F., Thomas, V. A., Winske, D., Gosling, J. T., Farris, M. H., & Russell, C. T. (1993). Observational test of hot flow anomaly formation by the interaction of a magnetic discontinuity with the bow shock. *Journal of Geophysical Research*, *98*(A9), 15,319–15,330. https://doi.org/10.1029/93JA00792

Turner, D. L., Omidi, N., Sibeck, D. G., & Angelopoulos, V. (2013). First observations of foreshock bubbles upstream of Earth's bow shock: Characteristics and comparisons to HFAs. *Journal of Geophysical Research: Space Physics*, *118*, 1552–1570. https://doi.org/10.1002/jgra.50198

Valek, P. W., Thomsen, M. F., Allegrini, F., Bagenal, F., Bolton, S., Connerney, J., … Wilson, R. J. (2017). Hot flow anomaly observed at Jupiter's bow shock. *Geophysical Research Letters*, *44*, 8107–8112. https://doi.org/10.1002/2017GL073175

Wahlund, J.-E., Boström, R., Gustafsson, G., Gurnett, D. A., Kurth, W. S., Pedersen, A., … Müller-Wodarg, I. (2005). Cassini measurements of cold plasma in the ionosphere of Titan. *Science*, *308*(5724), 986–989. https://doi.org/10.1126/%20science.1109807

Wei, H. Y., Russell, C. T., Dougherty, M. K., Neubauer, F. M., & Ma, Y. J. (2010). Upper limits on Titan's magnetic moment and implications for its interior. *Journal of Geophysical Research*, *115*, E10007. https://doi.org/10.1029/2009JE003538

Went, D. R., Hospodarsky, G. B., Masters, A., Hansen, K. C., & Dougherty, M. K. (2011). A new semiempirical model of Saturn's bow shock based on propagated solar wind parameters. *Journal of Geophysical Research*, *116*, A07202. https://doi.org/10.1029/2010JA016349

Winske, D., & Omidi, N. (1993). Hybrid codes: Methods and applications. In H. Matsumoto, & Y. Omura (Eds.), *Computer space plasma physics: Simulation techniques and software* (Vol. 103, pp. 103–160). Tokyo: Terra Scientific.

Winske, D., & Omidi, N. (1996). A nonspecialist's guide to kinetic simulations of space plasmas. *Journal of Geophysical Research*, *101*(A8), 17,287–17,303. https://doi.org/10.1029/96JA00982

Zhang, H., Sibeck, D. G., Zong, Q.-G., Gary, S. P., Macfadden, J. P., Lason, D., … Angelopoulos, V. (2010). Time history of events and macroscale interactions during substorms observations of a series of hot flow anomaly events. *Journal of Geophysical Research*, *115*, A12235. https://doi.org/10.1029/2009JA015180

Zhang, H., Sibeck, D., Zong, Q. G., Omidi, N., Turner, D., & Clausen, L. N. (2013). Spontaneous hot flow anomalies at quasi-parallel shocks: 1. Observations. *Journal of Geophysical Research: Space Physics*, *118*, 3357–3363. https://doi.org/10.1002/jgra.50376